Supporting Information

Enhancement and Inversion of Absorptive Nonlinearity Induced by Topochemically Controlled Insulator-to-Metal Transition

Di Zhao[a], Duoduo Zhang[a], Yuting Yang[a], Xiaojie Yin[c,d], Xiaofeng Liu[a,b]*, Jianrong Qiu[e]

[a]*School of Materials Science and Engineering, Zhejiang University, Hangzhou 310027, China*

[b]*Wuhan National Laboratory for Optoelectronics, Wuhan 430074, China*

[c]*State Key Laboratory of Integrated Optoelectronics, Institute of Semiconductors, Chinese Academy of Sciences, Beijing 100083, China*

[d]*Shijia Photonics Technology, Hebi 458030, China*

[e]*State Key lab of Modern Optical Instrumentation and College of Optical Science and Engineering, Zhejiang University, Hangzhou 310027, China*

*E-mail: xfliu@zju.edu.cn

Contents

1. **Additional structural and optical characterizations**
   - **1.1 SEM and TEM characterizations**
   - **1.2 Optical characterizations**
   - **1.3 Electronic band structure**
2. **Mathematical formulations and additional NLO measurements**
   - **2.1 Mathematical formulations**
   - **2.2 Power-dependent Z-scan measurement**
   - **2.3 List of NLO parameters and comparison with contemporary materials**
3. **Pulse laser setup and additional experimental results**
   - **3.1 Pulse laser setup**
   - **3.2 Additional results on pulse laser generation**
   - **3.3 Comparison of pulse laser performances**

1. Additional structural and optical characterizations

1.1 SEM and TEM characterizations

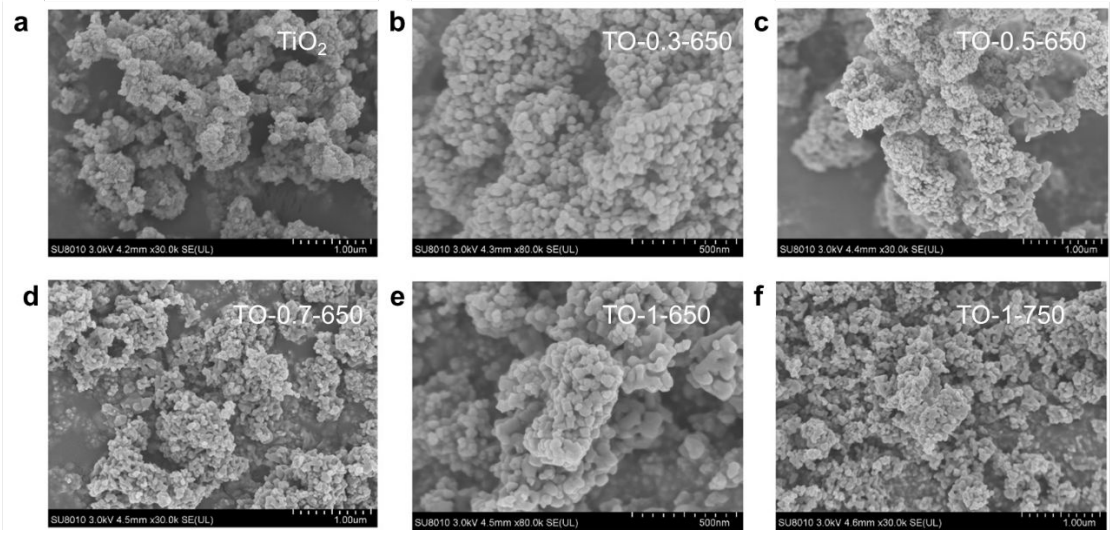

Figure S1. SEM images of different samples obtained at different conditions.

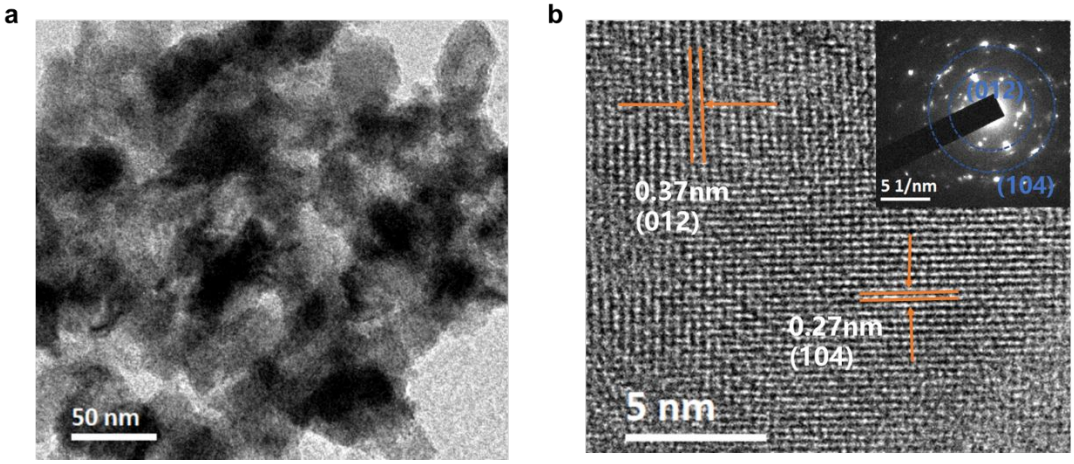

Figure S2. (a) TEM images of and (b) HR-TEM images of TO-1-750. Inset is the SAED pattern, confirming that formation of Ti_2O_3 phase with an orthorhombic structure.

The morphology of the samples as observed by SEM indicate agglomeration of the NPs, while these oxide NPs can be dispersed in water with the assistance of ultrasonic agitation to form stable colloid (as shown in Figure S3). For the sample obtained at a higher reaction temperature (750 °C), strong aggregation of the NPs can be observed

due to a sintering effect. From the SEAD pattern, the crystal phase in sample TO-1-750 is identified to be orthorhombic Ti_2O_3, which is in consistence with the XRD result (see Figure 2f in the main text).

1.2 Optical characterizations

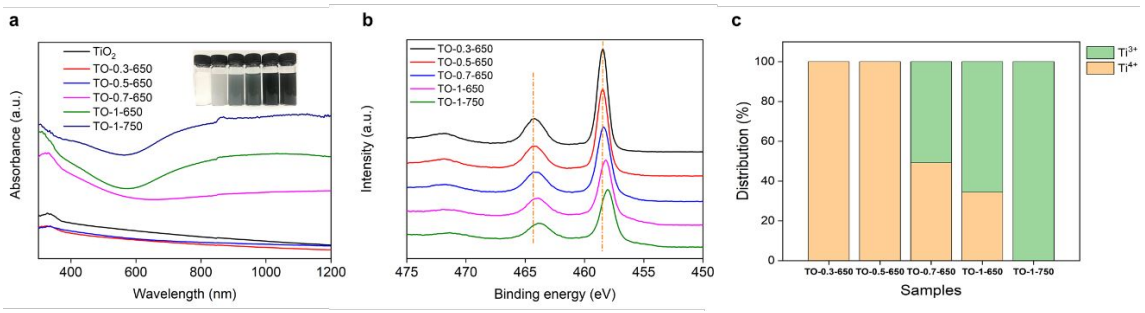

Figure S3. (a) Absorption spectra of the aqueous dispersions of the samples (concentration: 0.5wt%). Inset is the photographs of the dispersions. (b) Comparison of the Ti-2p high resolution XPS spectra for different samples. (c) The fraction of Ti^{3+} and Ti^{4+} for different samples calculated from the XPS spectra.

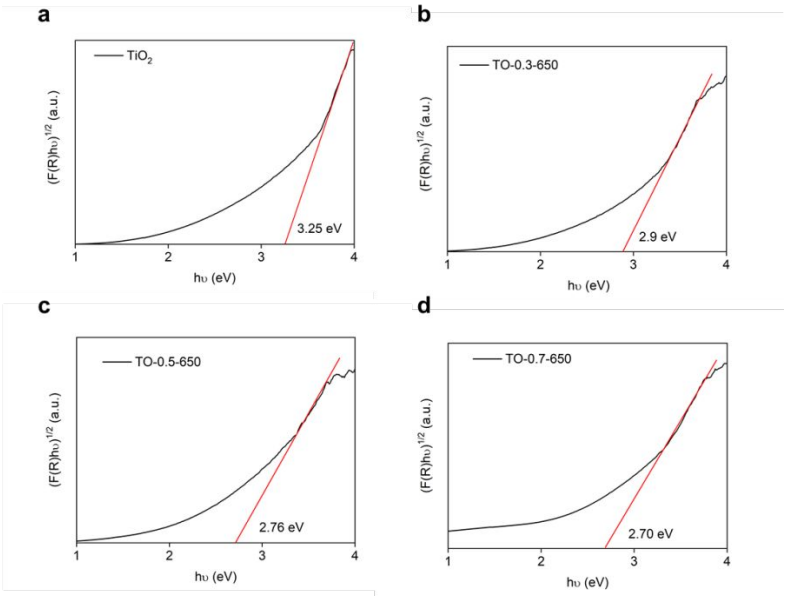

Figure S4. Tauc plot based on the reflectance spectra (after conversion by the Kubelka-Munk function, with $F(R) = \frac{(1-R)^2}{2R}$), where R is the reflectance) for different samples: (a) anatase TiO_2; (b) TO-0.3-650; (c) TO-0.5-650; (d) TO-0.7-650.

The absorption spectra measured for the colloidal dispersion of the samples show

clear transition of optical properties with the increase of oxygen deficiency. Especially, for samples TO-0.5-650 and TO-0.7-650, a broadened absorption band located in the near infrared (NIR) region is observed, which can be explained by the localized plasmon resonance arise from conduction electrons in metallic materials. This result agrees with the XRD and XPS that confirm the formation of metallic Magnéli phases (Ti_2O_3 and Ti_4O_7). From samples with a low level of oxygen deficiency (TO-0.3-650, TO-0.5-650 and TO-0.7-650), we observe a clear decrease of bandgap values from 3.25 eV (for anatase) to 2.70 eV (TO-0.7-650) from the Tauc plot presented in Figure S4.

1.3 Electronic band structure

We note that DFT calculation could underestimate the bandgap values, while the results can be used in the semi-quantitative manner for the analysis of the optical properties and nonlinear optical response. As can be seen in Figure 4b, the oxygen vacancies in the anatase structure create an isolated band below the conduction band and this is supported by the decrease in optical bandgap for samples with increasing level of oxygen deficiency. For Ti_4O_7 and Ti_2O_3, their electronic band structures confirm metallicity as the filling of Ti-3d band pushes Fermi level upward to cross the conduction band that are of primarily Ti-3d character (see Figure 4 in the main text).

2. Mathematical formulations and additional NLO measurements

2.1 Mathematical formulations

According to the nonlinear absorption theory,[1] the absorption coefficient $\alpha(I)$ consists

of the linear absorption coefficient α_0 and the nonlinear absorption coefficient α_{NL}, that is

$$\alpha(I) = \alpha_0 + \alpha_{NL} I \quad \text{(S1)}$$

and α_0 can be obtained by Lambert formula

$$\mathrm{T} = e^{-\alpha_0 L} \quad \text{(S2)}$$

The imaginary part ($Im\chi^{(3)}$) and quality factor (Figure of Merit, FOM) of the third-order nonlinear susceptibility are expressed as

$$Im\,\chi^{(3)} = (10^{-7} c\lambda n^2)\alpha_{NL}/(96\pi^2) \quad \text{(S3)}$$

$$FOM = \left|\frac{Im\,\chi^{(3)}}{\alpha_0}\right| \quad \text{(S4)}$$

where c is the speed of light and n is the linear refractive index of the material.

According to the well-established NLO theory, the RSA curves of the open aperture Z-scan for n-photon absorption can be fitted by:[2]

$$T_{nPA} = 1 - \frac{1}{n^{3/2}}\alpha_n (I_0)^{n-1} L_{eff}^{(n)} \quad \text{(S5)}$$

where $L_{eff}^{(n)}$ is the effective path length in the sample for n-photon absorption (nPA) and is given as $L_{eff} = \left(1 - e^{-(n-1)\alpha_0 L}\right)/[(n-1)\alpha_0]$ (L is sample thickness).

The 2PA cross-section (σ_2) is calculated according to:[3]

$$\sigma_2 = \frac{h\nu\alpha_{NL}}{N_0} \quad \text{(S6)}$$

The transient process of saturable absorption was fitted by double exponential decay function

$$T(t,\omega) = a(\omega) \cdot e^{-t/\tau_1} + b(\omega) \cdot e^{-t/\tau_2} + c(\omega) \quad \text{(S7)}$$

where a and τ_1 represent the decay coefficient and decay time constant of the fast state process. b and τ_2 represent the decay coefficient and decay time constant of slow state

process, respectively. *c* represents the linear transmittance of the sample at different wavelengths.

2.2 Power-dependent Z-scan measurement

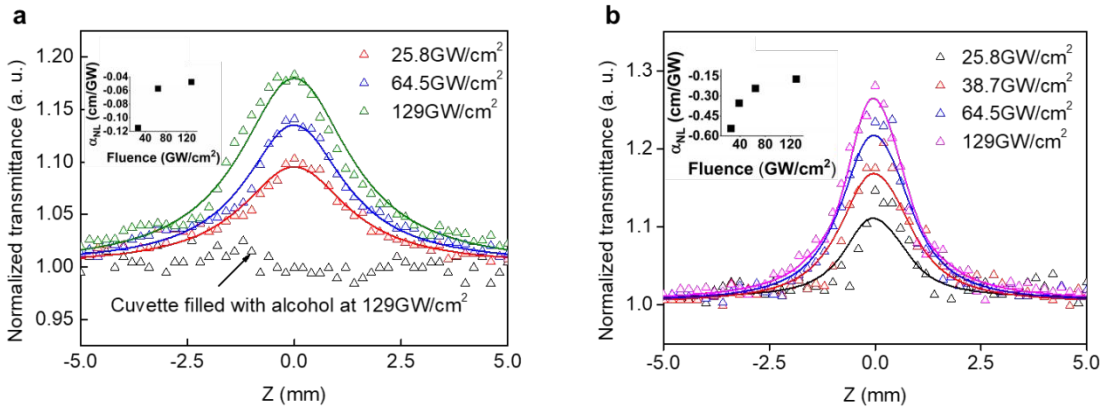

Figure S5. Z-scans curves under different optical power density for (a) TO-0.7-650; (b) TO-1-650 dispersed in alcohol.

It is observed from Figure S5 the transmittance change is dependent on the optical power density at the focus. By fitting the Z-scan curves we obtained the nonlinear absorption coefficients for different power densities, which are given in the insets. For both samples we observe an increase in α_{NL} with the rise of power density, which can be generally explained by the saturation effect.

2.3 List of NLO parameters and comparison with contemporary materials

Table S1. Calculation of NLO parameters for the examined samples.

Sample	T (%)	α_0 (cm^{-1})	α_{NL} (cm/ GW)	$Im\chi^3$ (esu)	FOM (cm·esu)
MT-0.3	81.4	2.06	0.0207	1.32×10^{-14}	6.41×10^{-15}
MT-0.5	73.3	3.11	-0.0337	-2.16×10^{-14}	6.95×10^{-15}
MT-0.7	70.0	3.57	-0.0475	-3.04×10^{-14}	8.52×10^{-15}
MT-1	32.3	11.30	-0.172	-1.10×10^{-13}	9.73×10^{-15}
MT-1-750	31.5	11.50	-0.248	-1.59×10^{-13}	-1.38×10^{-14}

Table S2. List of measured NLO optical properties of noble metal NPs and other systems.

Materials	Laser parameters	α_{NL} (cm/ GW)	$Im\chi^3$ (esu)	FOM (cm·esu)
TO-1	1030nm, 230fs	-0.172	-1.10×10^{-13}	9.73×10^{-15}
TO-1-750	1030nm, 230fs	-0.248	-1.59×10^{-13}	-1.38×10^{-14}
Au nanorods[4]	800nm, 220fs	-1.5	-1.2×10^{-12}	3.00×10^{-14}
$MoSe_2$[5]	800nm, 100fs	-0.017	-0.98×10^{-14}	1.88×10^{-15}
MoS_2[6]	800nm, 100fs	-0.0046	-2.52×10^{-15}	1.06×10^{-15}
BP[7]	800nm, 100fs	-0.0682	9.92×10^{-14}	8.81×10^{-15}
B-AsP[8]	1800nm, 100fs	-0.23	—	—
Ni-MOFs[9]	1060nm, 95fs	-0.039	-3.3×10^{-14}	—

The results given in Table S1 show the calculated NLO parameters based on the fitting of Z-scan curves. In addition to the inversion of NLO absorption coefficient (α_{NL}), it is clear that the NLO parameters are dependent on the linear absorption. However, the *FOM* values of our samples and other 2D materials all fall into the range of 10^{-14} - 10^{-15}.

3 Pulse laser setup and additional experimental results

3.1 Pulse laser setup

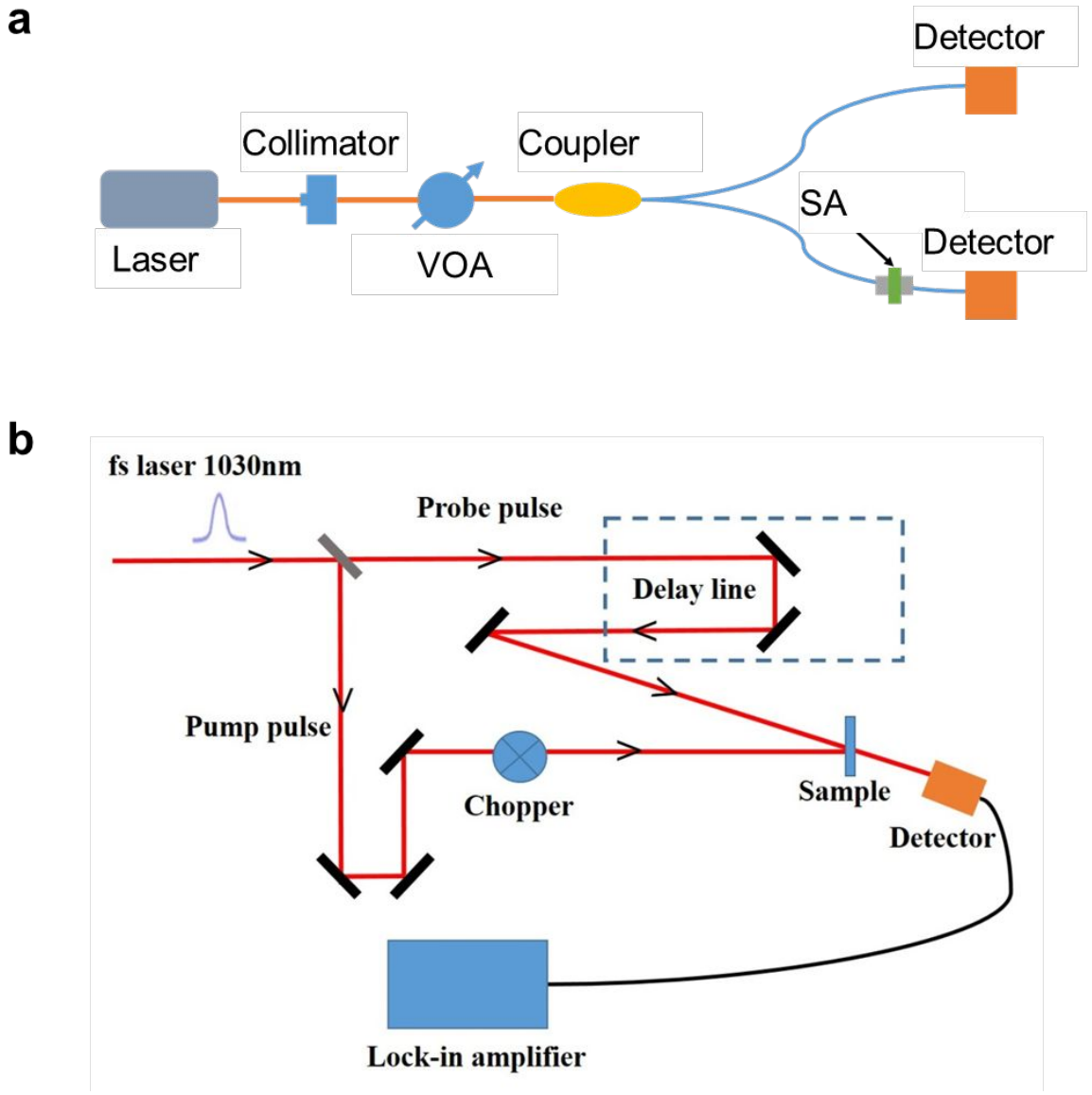

Figure S6. Schematic diagram of (a) the I-scan setup for the measurement of NLO absorption of the samples; (b) the pump-probe experimental setup.

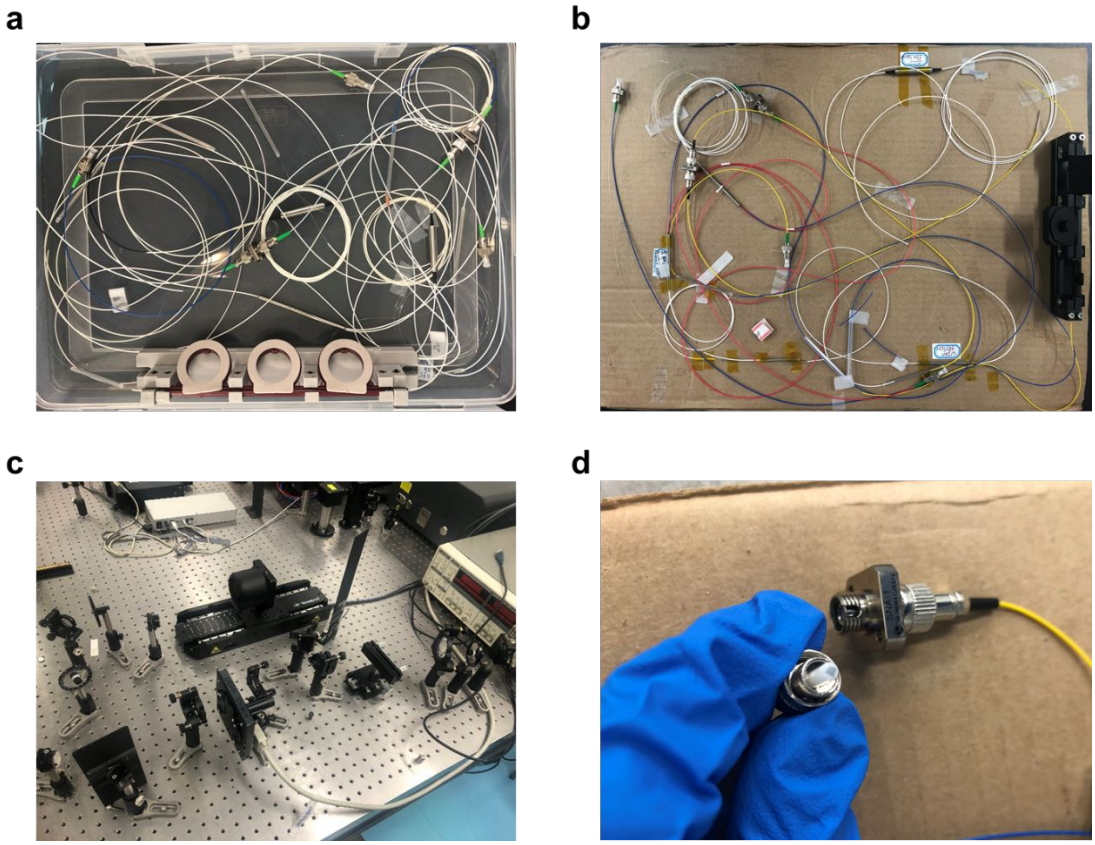

Figure S7. Photograph of (a) the 1.0 μm fiber laser; (b) the 1.5 μm fiber laser. (c) the degenerate pump-probe setup; (d) Photograph of a PVA/NPs film attached onto the facet of a fiber connector. The schematic diagram for (a) is given in the main text (Figure 5c).

In the present work, the I-scan measurement can be considered as an alternative method for determining the NLO absorption of samples. The results of I-scan are in fact more relevant to pulse laser application as it directly measures the modulation depth (NLO absorption) based on power-dependent transmission at the laser wavelength.

3.2 Additional results on pulse laser generation

A. Q-switched pulse output at 1.5 μm based on the switch fabricated from TO-0.7-650

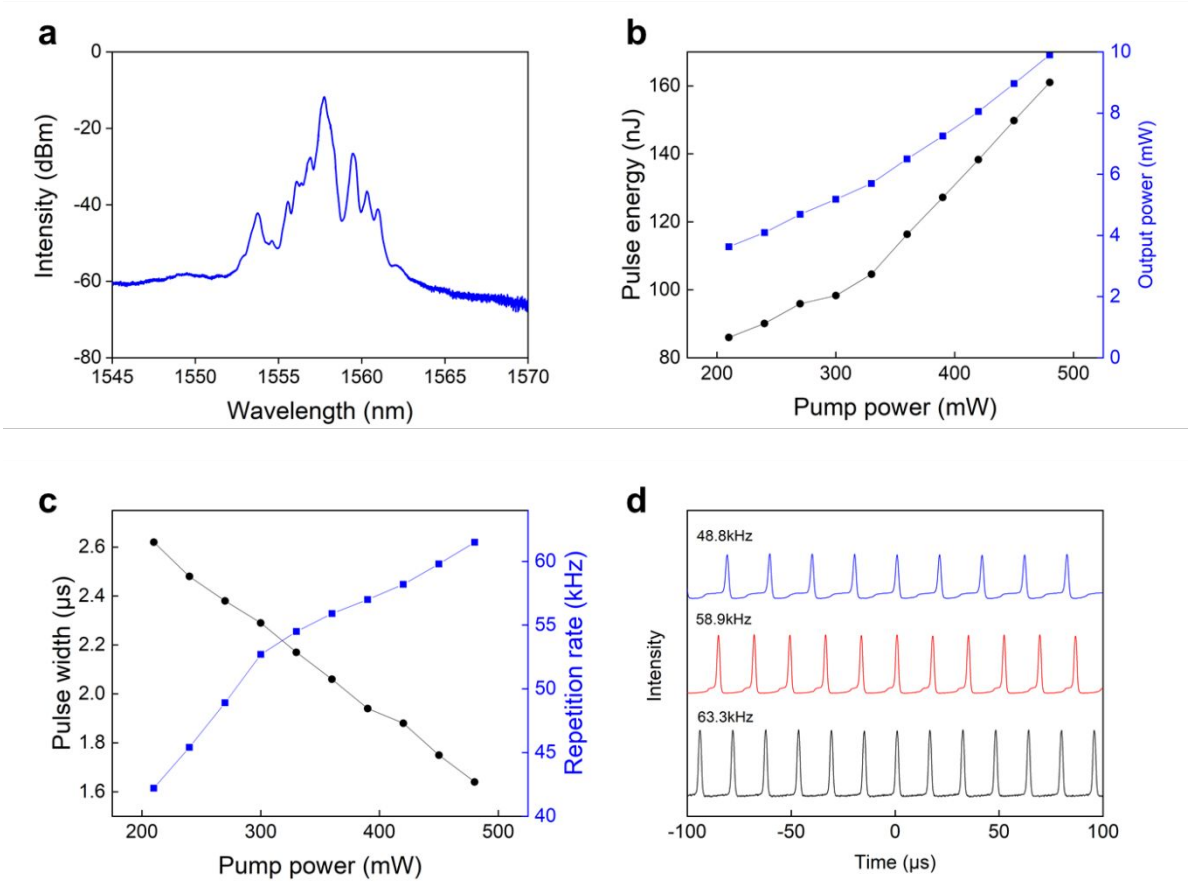

Figure S8. Q-switched pulse laser output based on the switch fabricated from TO-0.7-650: (a) the Q-switched laser spectrum; (b) pulse energy and output power versus pumping power; (c) pulse width and repetition rate versus pumping power; (d) pulse trains with different repetition rate.

In our laser experiments, we fabricated 5 optical switches using the examined samples and Q-switched pule generation at 1.5 μm is only observed for the optical switch fabricated from TO-0.7-650. As can be seen from Figure S8, the maximum output power reaches 10 mW at the pumping power of around 475 mW.

B. Q-switching pulse output at 1.5 μm based on the switch fabricated from TO-1-750

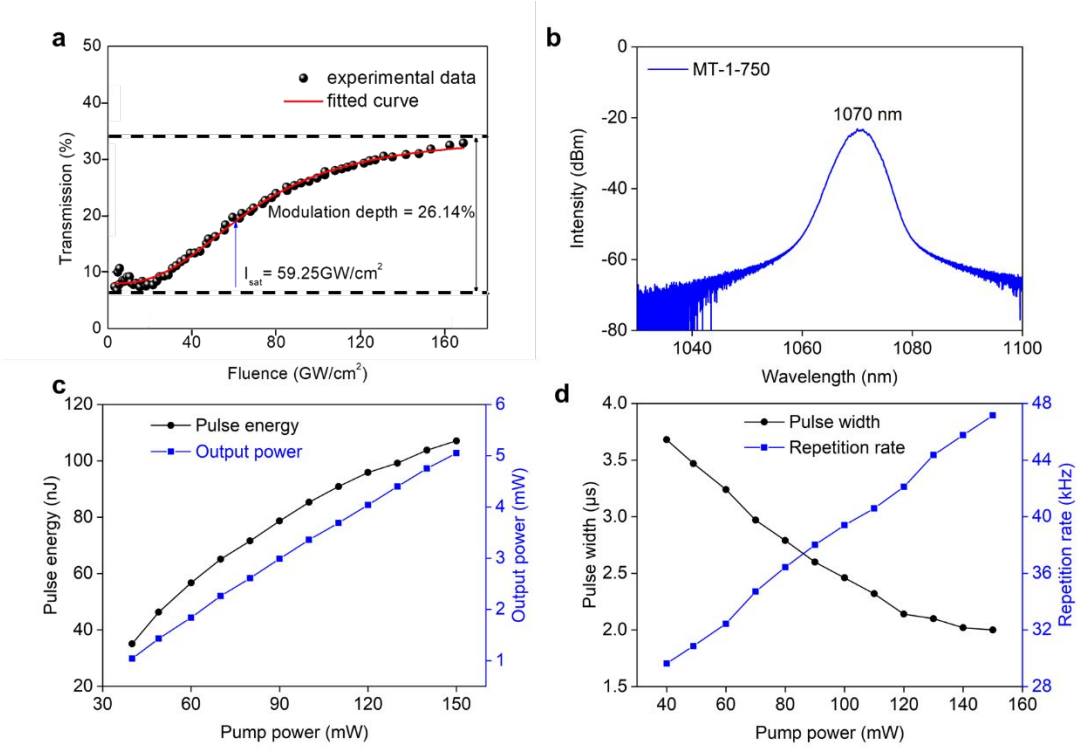

Figure S9. Q-switched pulse laser output based on the switch fabricated from TO-1-750: (a) NLO absorption measured by I-scan method, recording a modulation depth of 26.14%; (b) the Q-switched laser spectrum; (c) pulse energy and output power versus pumping power; (d) Pulse width and repetition rate versus pumping power.

C. Mode-locked pulse output at 1.0 μm based on the switch fabricated from TO-1-750

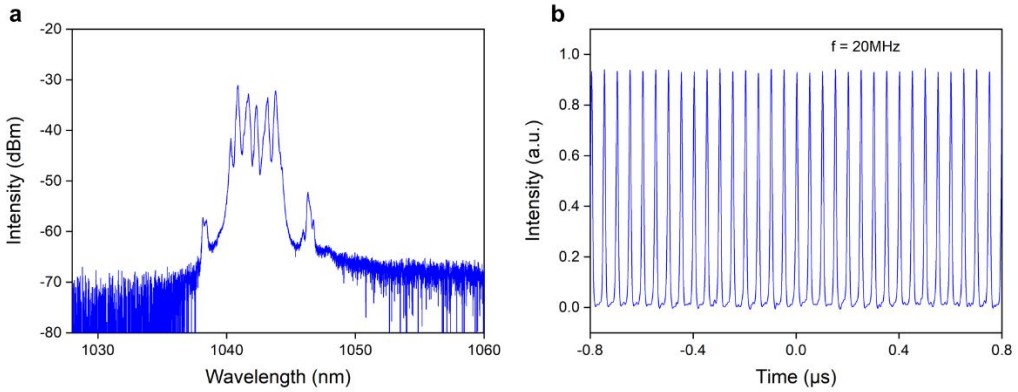

Figure S10. Mode-locked pulse laser output based on the switch fabricated from TO-1-750: (a) laser spectrum at 1.0 μm; (b) pulse train with a repletion rate of 20 MHz.

From Figures S9 and S10, the optical switch fabricated from sample TO-1-750 can drive both Q-switched and mode-locked pulse generation at 1.0 μm. This is the only optical switch that realized mode-locked pulse output in our experiment. The differences in the performances of the fabricated switches can be explained by the variation in linear and nonlinear optical properties in the series of Ti-oxide NP samples.

3.3 Comparison of pulse laser performances

Table S3. Comparison of pulse laser performances (Q-switching) with lasers driven by optical switches made from other materials.

Optical switch	Wavelength	Pulse width	Pulse energy	Output power	Repetition rate	Ref.
MoS_2	1066.5 nm	5.8 μs	32.6 nJ	0.9 mW	28.9 kHz	[10]
$MoSe_2$	1060 nm	2.8 μs	116 nJ	8.72 mW	74.9 kHz	[11]
BP	1064.7 nm	2.0 μs	11.7 nJ	3.2 mW	76 kHz	[12]
Bi_2Te_3	1056.5 nm	1.0 μs	38.3 nJ	2.95 mW	77 kHz	[13]
Bi_2Se_3	1067 nm	1.95 μs	17.9 nJ	0.46 mW	29.1 kHz	[14]
Fe_2O_3	1038 nm	2.2 μs	38.2 nJ	2.6 mW	28 kHz	[15]
Fe_3O_4	1030 nm	1.63 μs	50.3 nJ	4.98 mW	102.2 kHz	[16]
TO-1	**1068 nm**	**1.05 μs**	**84.4 nJ**	**8.9 mW**	**105.5 kHz**	**this work**
TO-1-750	**1070 nm**	**1.0 μs**	**107 nJ**	**5.05 mW**	**47.2 kHz**	**this work**

From the comparison given in Table S3, one peculiar feature of the optical switches developed here is that they enable much higher output power (and pulse energy) as compared with the pulse laser systems driven by optical switches made from other materials. This result indicates high stability of the developed optical switches, which is benefited from the high stability of the materials we developed.

References

(1) Woodward, R. I.; Kelleher, E. J. R. 2d Saturable Absorbers for Fibre Lasers. *Appl. Sci-Basel* **2015,** *5*, 1440-1456.

(2) Gu, B.; Huang, X. Q.; Tan, S. Q.; Wang, M.; Ji, W. Z-Scan Analytical Theories for Characterizing Multiphoton Absorbers. *Appl. Phys. B-Lasers O* **2009,** *95*, 375-381.

(3) Corrêa, D. S.; De Boni, L.; Misoguti, L.; Cohanoschi, I.; Hernandez, F. E.; Mendonça, C. R. Z-Scan Theoretical Analysis for Three-, Four- and Five-Photon Absorption. *Opt. Commun.* **2007,** *277*, 440-445.

(4) Elim, H. I.; Yang, J.; Lee, J. Y.; Mi, J.; Ji, W. Observation of Saturable and Reverse-Saturable Absorption at Longitudinal Surface Plasmon Resonance in Gold Nanorods. *Appl. Phys. Lett.* **2006,** *88*.

(5) Wang, G.; Liang, G.; Baker-Murray, A. A.; Wang, K.; Wang, J. J.; Zhang, X.; Bennett, D.; Luo, J.-T.; Wang, J.; Fan, P.; et al. Nonlinear Optical Performance of Few-Layer Molybdenum Diselenide As a Slow-Saturable Absorber. *Photonics Res.* **2018,** *6*, 674-680.

(6) Wang, K.; Wang, J.; Fan, J.; Lotya, M.; O'Neill, A.; Fox, D.; Feng, Y.; Zhang, X.; Jiang, B.; Zhao, Q.; et al. Ultrafast Saturable Absorption of Two-Dimensional MoS_2 Nanosheets. *Acs Nano* **2013,** *7*, 9260-9267.

(7) Lu, S.; Ge, Y.; Sun, Z.; Huang, Z.; Cao, R.; Zhao, C.; Wen, S.; Fan, D.; Li, J.; Zhang, H. Ultrafast Nonlinear Absorption and Nonlinear Refraction in Few-Layer Oxidized Black Phosphorus. *Photonics Res.* **2016,** *4*, 286-292.

(8) Shu, Y.; Guo, J.; Fan, T.; Xu, Y.; Guo, P.; Wang, Z.; Wu, L.; Ge, Y.; Lin, Z.; Ma, D.; et al. Two-Dimensional Black Arsenic Phosphorus for Ultrafast Photonics in near- and Mid-Infrared Regimes. *ACS Appl. Mater. Interfaces* **2020,** *12*, 46509-46518.

(9) Jiang, X.; Zhang, L.; Liu, S.; Zhang, Y.; He, Z.; Li, W.; Zhang, F.; Shi, Y.; Lü, W.; Li, Y.; et al. Ultrathin Metal–Organic Framework: An Emerging Broadband Nonlinear Optical Material for Ultrafast Photonics. *Adv. Opt. Mater.* **2018,** *6*, 1800561.

(10) Luo, Z.; Huang, Y.; Zhong, M.; Li, Y.; Wu, J.; Xu, B.; Xu, H.; Cai, Z.; Peng, J.; Weng, J. 1-, 1.5-, and 2-μm Fiber Lasers Q-Switched by a Broadband Few-Layer MoS_2 Saturable Absorber. *J. Lightwave Technol.* **2014,** *32*, 4077-4084.

(11) Woodward, R. I.; Howe, R. C. T.; Runcorn, T. H.; Hu, G.; Torrisi, F.; Kelleher, E. J. R.; Hasan, T. Wideband Saturable Absorption in Few-Layer Molybdenum Diselenide ($MoSe_2$) for Q-Switching Yb-, Er- and Tm-Doped Fiber Lasers. *Opt. Express* **2015,** *23*, 20051-20061.

(12) Huang, K.-X.; Lu, B.-L.; Li, D.; Qi, X.-Y.; Chen, H.-W.; Wang, N.; Wen, Z.-R.; Bai, J.-T. Black Phosphorus Flakes Covered Microfiber for Q-Switched Ytterbium-Doped Fiber Laser. *Appl. Opt.* **2017,** *56*, 6427-6431.

(13) Lee, J.; Koo, J.; Chi, C.; Lee, J. H. All-Fiberized, Passively Q-Switched 1.06 μm Laser Using a Bulk-Structured Bi_2Te_3 Topological Insulator. *Journal of Optics* **2014,** *16*, 085203.

(14) Luo, Z.; Huang, Y.; Weng, J.; Cheng, H.; Lin, Z.; Xu, B.; Cai, Z.; Xu, H. 1.06

μm Q-Switched Ytterbium-Doped Fiber Laser Using Few-Layer Topological Insulator Bi_2Se_3 as a Saturable Absorber. *Opt. Express* **2013,** *21*, 29516-29522.

(15) Mao, D.; Cui, X.; He, Z.; Lu, H.; Zhang, W.; Wang, L.; Zhuang, Q.; Hua, S.; Mei, T.; Zhao, J. Broadband Polarization-Insensitive Saturable Absorption of Fe_2O_3 Nanoparticles. *Nanoscale* **2018,** *10*, 21219-21224.

(16) Li, L.; Lv, R.; Liu, S.; Chen, Z.; Wang, J.; Wang, Y.; Ren, W.; Liu, W. Ferroferric-Oxide Nanoparticle Based Q-Switcher for a 1 μm Region. *Opt. Mater. Express* **2019,** *9*, 731-738.